Chemistry
A European
Journal

Chemistry Europe
European Chemical Societies Publishing

## Accepted Article

**Title:** Amorphous calcium phosphates: Solvent-controlled growth and stabilization through the Epoxide Route

**Authors:** Matias Jobbagy, Paula Borovik, Víctor Oestreicher, and Cristián Huck-Iriart



**To be cited as:** *Chem. Eur. J.* 10.1002/chem.202005483

**Link to VoR:** https://doi.org/10.1002/chem.202005483

WILEY-VCH

10.1002/chem.202005483

# Amorphous Calcium Phosphates: Solvent-controlled Growth and Stabilization through the Epoxide Route

Paula Borovik[a,γ,±], Dr. Víctor Oestreicher[a,γ,≠*], Prof. Cristián Huck-Iriart[b] and Prof. Matías Jobbágy[a*]

[a]INQUIMAE-DQIAQF, Facultad de Ciencias Exactas y Naturales, Universidad de Buenos Aires. Ciudad Universitaria, Pab. II (1428), Buenos Aires, Argentina

[b]Escuela de Ciencia y Tecnología, Universidad Nacional de San Martín, CONICET, 25 de mayo 1650, San Martín (1650), Buenos Aires, Argentina

[±]Current address: Gerencia Química & Instituto de Nanociencia y Nanotecnología, Centro Atómico Constituyentes, Comisión Nacional de Energía Atómica, CONICET, Av. Gral. Paz 1499, San Martín (1650), Buenos Aires, Argentina

[≠]Current address: Instituto de Ciencia Molecular (ICMol), Universidad de Valencia, Catedrático José Beltrán 2, Paterna (46980), Valencia, Spain

[γ]Both authors contributed equally to this work

Corresponding authors: victor.oestreicher@uv.es; jobbag@qi.fcen.uba.ar

*Calcium phosphates stand among the most promising nanobiomaterials in key biomedical applications as bone repairment, signalling or drug/gene delivery. Intrinsic properties as crystalline structure, composition, particle shape and size define the successful use of these phases. Among them, metastable amorphous calcium phosphate (ACP) is currently gaining particular attention due to its inherently high reactivity in solution, which is crucial in bone development mechanisms. However, the preparation of this highly desired (bio)material with control over its shape, size and phase purity Calcium phosphates stand among the most promising nanobiomaterials in key biomedical applications as bone repairment, signalling or drug/gene delivery. Their intrinsic properties as crystalline structure, composition, particle shape and size define their successful use. Among these compounds, metastable amorphous calcium phosphate (ACP) is currently gaining particular attention due to its inherently high reactivity in solution, which is crucial in bone development mechanisms. However, the preparation of this highly desired (bio)material with control over its shape, size and phase*

10.1002/chem.202005483

*purity remains as a synthetic challenge. Herein, we have adapted the Epoxide Route for the synthesis of pure and stable ACP colloids. By using biocompatible solvents such as ethylene glycol and/or glycerine we are able to avoid the natural tendency of ACP to maturate into more stable and crystalline apatites. Moreover, this procedure offers size control, ranging from small nanoparticles (60 nm) to micrometric spheroids (>500 nm). The eventual fractalization of the internal mesostructured can be tuned, by simply adjusting the composition of the ethylene glycol:glycerine solvent mixture. These findings introduce the use of green solvents as a new tool to control crystallinity and/or particle size in the synthesis of nanomaterials, avoiding the use of capping agents and preserving the natural chemical reactivity of the pristine surface. remains as a synthetic challenge. Herein, we have adapted the Epoxide Route for the synthesis of pure and stable ACP colloids. By using biocompatible solvents such as ethylene glycol and/or glycerine we are able to avoid the natural tendency of ACP to maturate into more stable and crystalline apatites. Moreover, this procedure offers size control, ranging from small nanoparticles (60 nm) to micrometric spheroids (>500 nm). The eventual fractalization of the internal mesostructured can be tuned, by simply adjusting the composition of the ethylene glycol:glycerine solvent mixture. These findings introduce the use of green solvents as a new tool to control crystallinity and/or particle size in the synthesis of nanomaterials, avoiding the use of capping agents and preserving the natural chemical reactivity of the pristine surface.*

## Introduction

Nanotextured calcium phosphates and their complex transformations are permanently studied from a fundamental point of view[1] since they play a key biological role in osteogenesis[2] and the constitution of hard tissues in vertebrates.[3] In addition, these inherently biocompatible compounds stand among the preferred building blocks for the development of advanced biomedical materials, finding applications beyond bone repairment,[4] as drug or gene delivery.[5] [6] [7] Moreover, due to their countless industrial uses, these nanophases belong to the most massively produced nanoparticles.[8]

Depending on the desired application, these building blocks must fulfil several requirements including controlled shape, size, composition and crystalline structure.[9] Among the reported phases, metastable ones in particular (such as the amorphous calcium phosphate (**ACP**),[10] [11] are gaining increasing attention due to their intrinsic high reactivity in solution.[6] Subsequently, it plays a key role in bone development mechanism[1] and its potential use in biomedical applications,[12] including advanced biomimetic[13] or bioinspired[14] composites. However, metastable amorphous phases as **ACP** could be difficult to isolate in pure forms and often require additional stabilization strategies[15] ranging from bulk isomorphic substitution[16] with other divalent cations such as Mg, Sr and Zn,[17] to surface functionalization[18] and passivation.[19] In addition, textural modifications as the agglomeration and subsequent surface area decrease demonstrated to be effective.[20] Notwithstanding, the aforementioned chemical or textural modifications can significantly alter the inherent *in vitro* or *in vivo* response of **ACP**, limiting the range of biomedical applications.

Mild chemical methods as homogeneous precipitation may offer a controlled nucleation and growth scenario for the preparation of calcium orthophosphates, eventually resulting in tuned composition and texture.[21] The first reports were based on the homogenous alkalinization driven by thermal hydrolysis of ammonia-releasing reagents (ARR), such as urea[22] or HMT,[23] succeed in certain textural control. However, in those cases, the hydrothermal conditions (temperatures higher than 90 ºC required to ensure the hydrolysis of the ARR at suitable rates), trigger the massive crystallization, which excludes the isolation of **ACP** phases. In addition, the concomitant carbonate tends to be massively incorporated in solids, as in the case of layered double hydroxides (LDHs),[24] giving birth to non-stoichiometric phases bearing variable calcium to phosphate ratios.[25] Enzymatically-driven growth at room temperature, employing phosphatases[26] [27] or ureases,[28] [29] [30] has been employed as an alternative to overcome this limitation. However, these approaches are expensive and hardly reproducible, limiting the possibilities of scaled up synthesis.

10.1002/chem.202005483

In recent years, the *Epoxide Route*[31] has emerged as a versatile tool to drive homogenous alkalinization and controlled precipitation in aqueous media, as an alternative to ARR-driven methods. *The Epoxide Route* is based on the nucleophilic attack on an epoxide ring at room temperature. It has been successfully employed to obtain diverse materials including colloidal inorganic layered hydroxides,[32] [33] [34] self-supported hydrogels,[35] [36] nanocomposites,[37] [38] hierarchical monoliths.[39] [40] [41] Also nanostructured films,[42] [43] hybrid[44] [45] or multivalent[46] 2D phases and metallic organic frameworks,[47] among others. In parallel with the aforementioned findings, several research teams reported that the addition of cosolvents in water-based precipitation process of calcium carbonates can dramatically affect the nature of these phases, modifying the particles' texture and their crystalline structure as well.[48] [49] [50] [51]

Thus, herein we introduce the synthesis of **ACP** particles with controlled size ranging from microns to nanometres through the *Epoxide Route*. Moreover, the control over the size was achieved without the use of surfactants, capping agents, and/or polymeric stabilizers, preserving the identity of the chemical surface of the **ACP** particles. Instead, the modulation of precursor solution's viscosity with green and biocompatible cosolvents such as ethylene glycol and/or glycerine allows an accurate size and textural control, and additionally avoids the transformation into non-desired phases. In addition, small angle X-ray scattering (SAXS) analysis alerts about changes in the inner mesostructuration of the samples as a function of the solvent's ratio. To the best of our knowledge this is the first report where viscosity permits a wide range control over the average particle size, introducing a green versatile and biocompatible tool for controlled nanomaterials' synthesis beyond calcium phosphate.

10.1002/chem.202005483

## Results and Discussion

In the search of suitable conditions to obtain pure and stable **ACP** nanoparticles, two main sets of experiments were performed according to the key aspects to be elucidated. Firstly, (*i*) the proposed method was explored in a range of concentrations, in order to screen and define the phase occurrence domain of **ACP** under the employed conditions. In addition, certain cases were inspected in more detail along the precipitation/aging process, in order to gain insights about the sequence and length of precipitation events. Secondly, (*ii*) the effect of cosolvents on the fate of **ACP** particles was explored to maximize their stability and tuning particle size as well. Therefore, the 'Results and Discussion' section is presented in two main sub-sections according to the main steps that followed our research (Scheme 1).

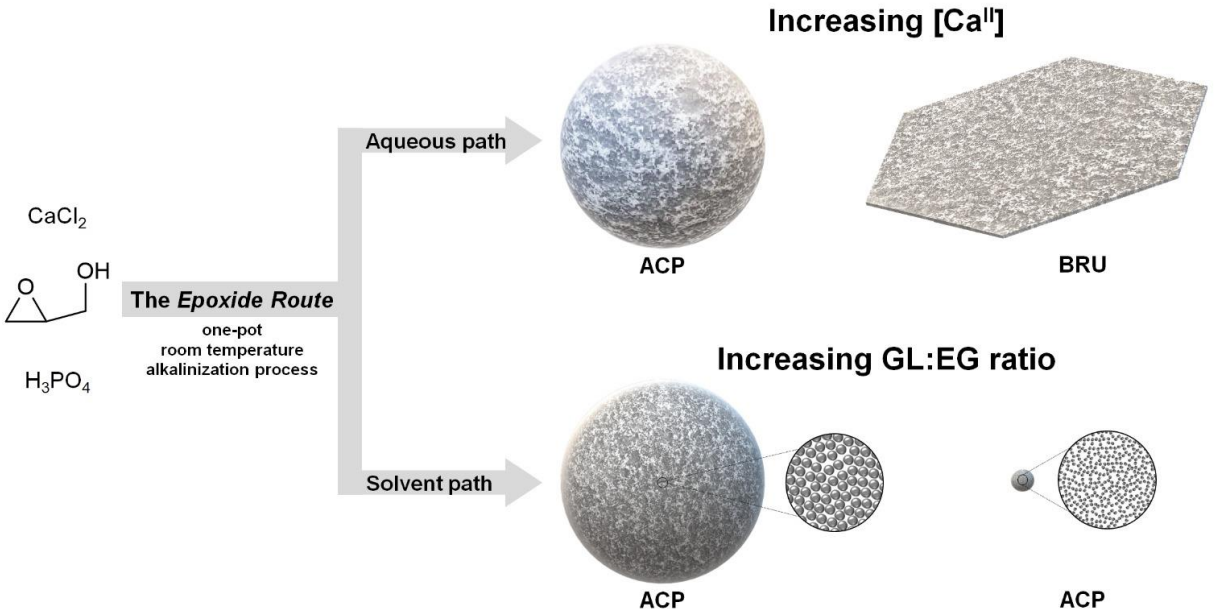


**Scheme 1.** The *Epoxide Route* was optimized to study the precipitation of calcium phosphate phases. Firstly, the effect of the reagents' concentration in aqueous media was performed. The increment of [$Ca^{II}$] drives the obtaining of *Brushite* (**BRU**) instead of *Hydroxyapatite* (**ACP**) (*i*). Secondly, the effect of biocompatible solvents, such as glycerine (GL) and ethylene glycol (EG), was studied. The use viscous cosolvent mixtures allow the precipitation of amorphous calcium phosphate (**ACP**), exclusively, while the GL:EG ratio can be employed to modulate either the size (from small 60 nm nanoparticles to large (>500 nm) spheroids) or the internal mesostructure, that varies from fractal-like nanoparticles to dense spheroids, when the GL is replaced by EG (*ii*).

**1. Phase stability and precipitation mechanisms.**

Under the characteristic mild conditions that the *Epoxide Route* offers, *in situ* experiments can be performed in order to study the precipitation sequence of growing phases. This approach has been employed to assess the growth mechanism and solubility (thermodynamic stability) of different layered materials, such as $Al^{III}$- and $Cr^{III}$-based layered double hydroxides (LDHs),[44] α-CoNi hydroxides[34] or α-$Co^{II}$ hydroxyhalides.[33] [52]In addition, a combination of *in situ* pH, UV-Vis and SAXS experiments have been useful to rationalize the role of the stabilizing agent (polymeric *vs.* cationic) in the gold nanoparticles formation.[37] These *in situ* continuous recordings of pH offer both kinetic and thermodynamic information. Hence, to shed light on the precipitation of calcium phosphate phases, *in situ* pH profiles were recorded at room temperature. All the synthesis along the present study were carried out employing an initial Ca:P ratio of 5:3, while the starting pH is defined by the initial phosphoric acid concentration (typically in the range pH = 2–3). Control experiments performed with phosphate salts, exclusively, resulted in no net alkalinization reaction (see Figure S1). Figure 1 depicts the pH profiles for two extreme precipitation scenarios defined at the lowest ([Ca] = 2 mM + [P] =1.2 mM) and the highest ([Ca] = 10 mM + [P] = 6 mM) concentrations explored herein, denoted as $[Ca+P]_{low}$ and $[Ca+P]_{high,}$ respectively. Moreover, an alkalinization control experiment containing NaCl and Gly was carried out to evaluate the inherent alkalinization rate profile, adjusted to drive the quantitative precipitation after few hours. Under this synthetic conditions, alkali release rate and subsequently, precipitation kinetics, depend on the product between Gly (epoxide) and chloride (nucleophile) concentrations.[31] Two other base consumption control experiments were also recorded in the absence of Ca employing 1.2 and 6 mM of phosphoric acid, $[P]_{low}$ and $[P]_{high,}$ respectively. For the NaCl–Gly control, once the Gly is added, the pH increases above pH values higher than 10 in *ca.* 30 min. In the cases of the [P] controls, both solutions require longer times to start increasing the pH, mainly due to the more acidic condition related to the addition of $H_3PO_4$. The higher the initial acid concentration, the lower the initial and the final maximum pH value and the slower the alkalinization rate. The shape of these pH profiles resembles typical titration curves, where the deceleration at *ca.* pH = 5 results from the buffering properties of the $H_2PO_4^-/HPO_4^{2-}$ acid-base couple, registering a maximum capacity at pH = 6.8–6.9 (see Figure S2). The higher the phosphoric acid concentration, the longer the buffered period lasts, as expected.

10.1002/chem.202005483

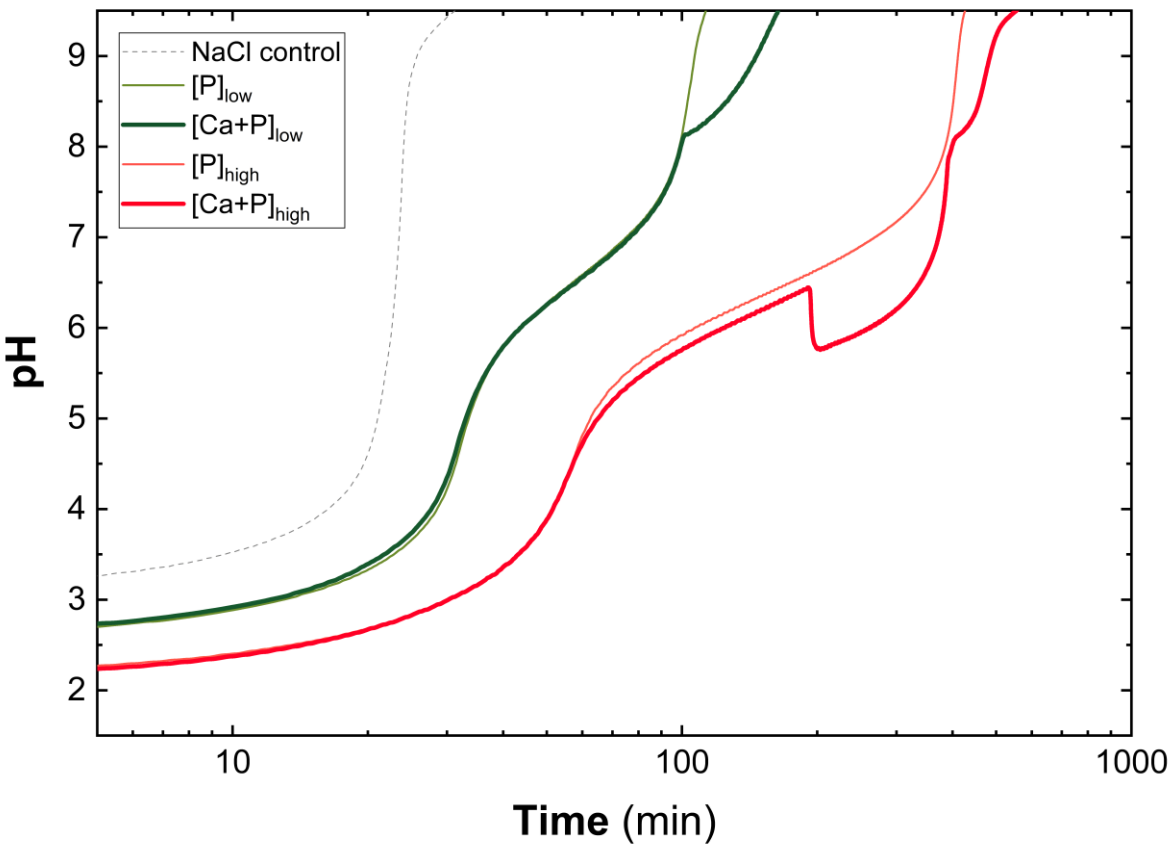


**Figure 1.** pH profiles recorded at room temperature employing aqueous solutions containing: [Gly] = 500 mM, [$Cl^-$] = 100 mM (NaCl control – dotted line), [$H_3PO_4$] = 1.2 ($[P]_{low}$ – green thin line) or 6 mM ($[P]_{high}$ – red thin line) or [Ca] = 2 ($[Ca+P]_{low}$ – green thick line) and 10 mM ($[Ca+P]_{high}$ – red thick line).

Regarding the precipitation, in the case of sample $[Ca+P]_{low}$ the pH profile practically follows the one recorded for $[P]_{low}$, suggesting that the presence of aqueous $Ca^{II}$ does not affect the alkalinization rate. Nevertheless, at pH = 8.1 an abrupt decrease in the alkalinization rate takes place in coincidence with the formation of a white solid, indicating the initiation of a precipitation event. After this point the pH curve of $[Ca+P]_{low}$ separates from the $[P]_{low}$ control one indicating that the chemical events associated with solid's formation (mainly taking place in presence of acid phosphate: $H_2PO_4^-/HPO_4^{2-}$ratios lower than 0.1. See Figure S3), are consuming significant net amounts of $OH^-$ moieties. Concerning the sample $[Ca+P]_{high}$, in the beginning the pH profile follows the one observed for $[P]_{high}$, as expected, up to a pH value of 4.5. Further alkalinization results in separated parallel curves where the slightly lower values recorded for $[Ca+P]_{high}$ can be assigned to the formation of Ca-phosphate pairs, that are inherently favoured to form at high concentrations. Further alkalinization reaches a critical pH value of around 6.4, where a white solid appears, and a sudden pH drop of 0.7 units takes place. Further alkalinization follows a precipitation *plateau* centred around pH = 5.8, were $H_2PO_4^-/HPO_4^{2-}$ratios are higher than 0.8 (see

Figure S3). At pH = 7 the profiles suddenly increase suggesting the end of the main precipitation event. Nevertheless, at pH around 8.1 a second base consumption event is noticeable. It is worth to mention that under this high concentration condition, *in situ* pH profiles help to identify base consuming events as for example the post-precipitation or dissolution/recrystallization of calcium phosphates phases, driven by the more basic conditions.

As a first step to characterize the obtained solids, FESEM inspection was performed considering the sequence and length of precipitation events. At pH *ca.* 9 (2.5h) sample $[Ca+P]_{low}$ consists of submicrometric/nanometric spherical particles of regular size with variable degree of coalescence. The rough surface indicates that nanoparticles result from the aggregation of primary units of a few nm in diameter (Figure 2A-B). However, at 24h (pH = 10.2) randomly oriented flakes, exhibiting thicknesses of a few nanometres, are noticed (Figure 2C-D). This observation alerts about a phase transformation and/or a recrystallization process that is taking place even at room temperature. In the case of sample $[Ca+P]_{high}$, at pH = 7 (*ca.* 6h) marked differences with respect to $[Ca+P]_{low}$ are revealed. At high calcium concentration the phase grows in the form of well-developed micrometric (>5 μm) crystalline platelets with sharply defined edges, evidencing a marked growth along preferential crystallographic directions (Figure 2E-F). Anew, at 24h (pH = 9.7) the occurrence of a massive post precipitation and/or surface reconstruction is noticeable. The pristine shape is mainly preserved while the former smooth surface of these micrometric platelets is totally covered by these nanoflakes (Figure 2G-H).

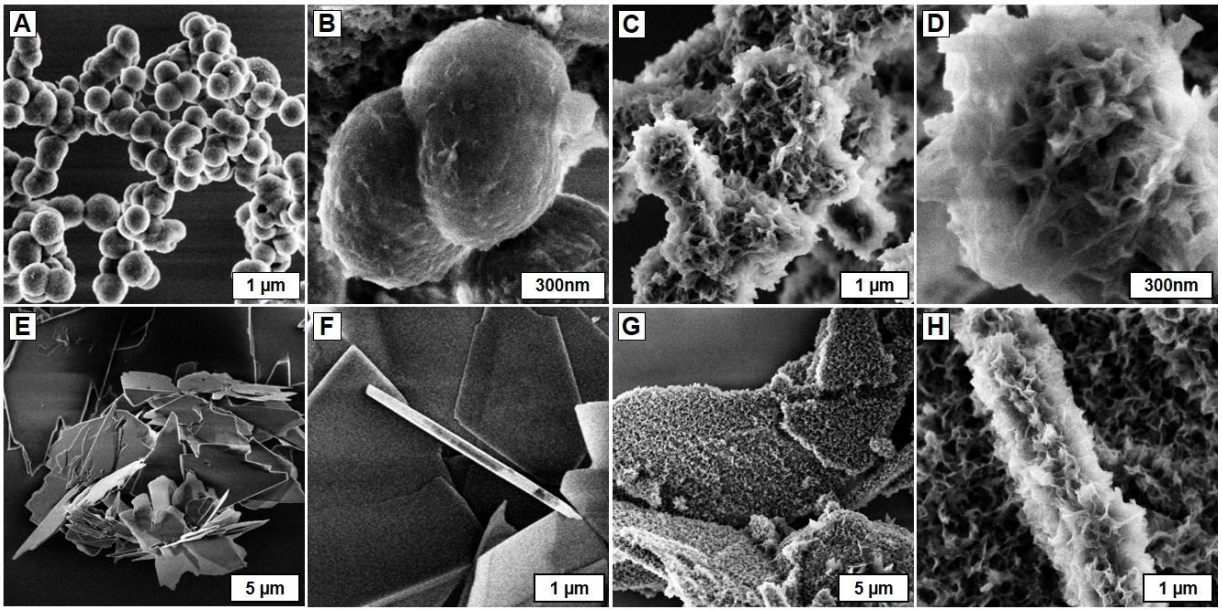


**Figure 2.** FESEM images recorded for samples $[Ca+P]_{low}$ (upper panel) at 2.5 (A-B) and 24h (C-D) and $[Ca+P]_{high}$ (lower panel) at 6 (E-F) and 24h (G-H), obtained by ageing at room temperature aqueous solutions containing: [Gly] = 500 mM, $[Cl^-]$ = 100 mM, $[H_3PO_4]$ = 1.2 or 6 mM and [Ca] = 2 or 10 mM.

10.1002/chem.202005483

In order to gain further insights into the crystallographic nature of these phases, PXRD was performed. Figure 3 depicts the PXRD patterns for both samples isolated at the two different stages. In the case of samples $[Ca+P]_{low}$, at 2.5 and 24h, no signals are observed, suggesting the growth of an amorphous phase at low calcium concentration. Thus, the ill-defined signal positioned at *2-theta* = 32.5º, mounted over the experimental background, could be related with amorphous calcium phosphate (**ACP** – $Ca_3(PO_4)_2 \bullet nH_2O$) inherently broad signal.[53] In the case of sample $[Ca+P]_{high}$, after 6h-long aging a highly crystalline phase is observed, where all the most intense peaks can be ascribed to *Brushite* (**BRU** – $CaHPO_4 \bullet 2H_2O$).[54] Furthermore, the marked prevalence of *020*, *040*, *060* and *080* reflections results from the occurrence of highly oriented crystals along the *0k0* direction and indicates highly anisotropic crystallographic growth as was reported for layered hydroxides prepared with the *Epoxide Route* (see Figure S4).[31] Nonetheless, after 24h, in the sample $[Ca+P]_{high}$ a new set of peaks are observed (located in the 25º < *2-theta* < 40º range, denoted with asterisk, see Figure 3), which can be ascribed to a nano crystalline *Hydroxyapatite* (**HAP** – $Ca_5(PO_4)_3(OH)$).

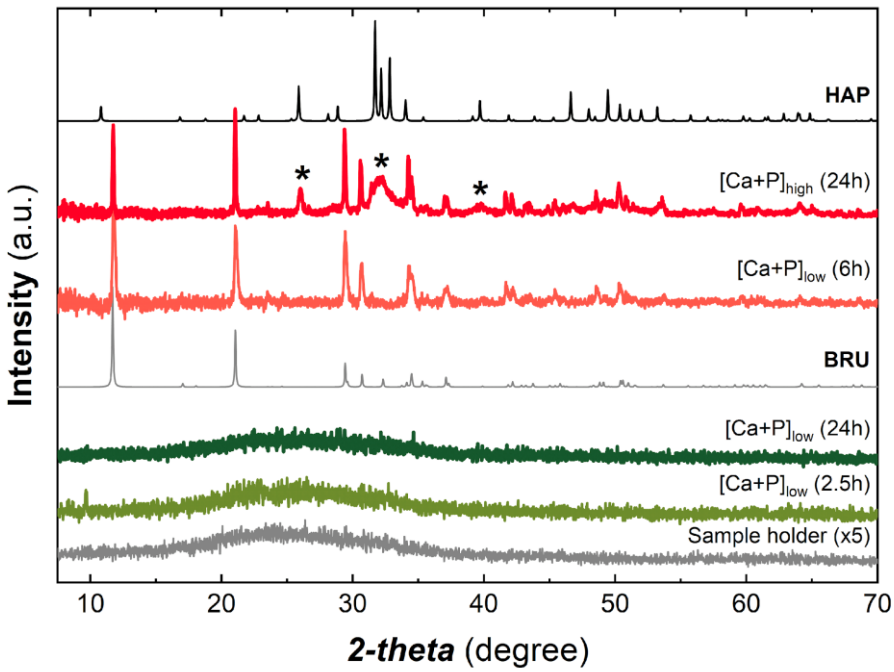


**Figure 3.** PXRD patterns for samples $[Ca+P]_{low}$ (2.5 and 24h) and $[Ca+P]_{high}$ (6 and 24h) at different times, obtained by ageing at room temperature aqueous solutions containing: [Gly] = 500 mM, $[Cl^-]$ = 100 mM, $[H_3PO_4]$ = 1.2 or 6 mM and [Ca] = 2 or 10 mM. Simulated PXRD patterns for *Brushite* (**BRU** – $CaHPO_4 \bullet 2H_2O$) and *Hydroxyapatite* (**HAP** – $Ca_5(PO_4)_3(OH)$) are also presented as references.

Once identified the crystallochemical nature of the obtained samples under each condition, it is worth to analyse the precipitation sequence observed along the alkalinization profiles. In the case of $[Ca+P]_{low}$, the precipitation is initiated once the solubility product of **ACP** phase[55] is reached, without the occurrence of oversaturation. The further transformation into **HAP** is a process that consumes a small absolute amount of base to be noticed (Eq. 1). Interestingly, in the case of $[Ca+P]_{high}$, the precipitation is also initiated once the solubility product of **ACP** phase is reached, however, after nucleation the pH descends to a value that matches the solubility of **BRU** and no longer the **ACP**, being the solid formation ruled by the formation of the former metastable phase. The second pH deceleration event implies a significant $OH^-$ consumption driven by the transformation of **BRU**, fed by the remnant free calcium ions, into **HAP** (Eq. 2).

$$3\ Ca_3(PO_4)_2\ (\mathbf{ACP}) + Ca^{2+} + 2\ OH^- \Rightarrow 2\ Ca_5(PO_4)_3OH\ (\mathbf{HAP}) \quad \mathbf{(1)}$$

$$3\ CaHPO_4{\bullet}2H_2O\ (\mathbf{BRU}) + 2\ Ca^{2+} + 4\ OH^- \Rightarrow Ca_5(PO_4)_3OH\ (\mathbf{HAP}) + 6\ H_2O \quad \mathbf{(2)}$$

Having established the marked effect of precursors' concentration on the obtained phases, additional experiments were carried out to define the highest calcium concentration in which the formation of **BRU** is prevented. Figure S5 depicts the PXRD patterns in the 2 – 10 mM calcium concentration range, where it is possible to observe that **BRU** prevails for concentrations of 6 mM or higher. However, both **ACP** and **BRU** phases are metastable and evolve partially or totally into the stable hydroxyapatite (**HAP**) phase, depending on the size of the initially obtained particles. In the case of **ACP**, the parent spheroidal[56] particles are no longer discernible, and eventually massively consumed after aging.[57] [58] [59] Nevertheless, depending on the Ca concentration, the **ACP** develops **HAP** or **HAP** + octacalcium phosphate (**OCP** – $Ca_8H_2(PO_4)_6 \bullet 5H_2O$) mixtures as well, as previously observed in related systems (see Figure S6).

In aqueous media, this process was reported to be strongly dependant on pH and strongly favoured at acidic conditions; under alkaline conditions both the induction time and conversion periods are extended to several hours.[60] The phases obtained after this initial screening can be summarized in the frame of a stability diagram, according to the reported solubility data of the observed phases.[61] Along the whole range of Ca concentrations explored herein, the less soluble **HAP** must precipitate at lower pH values, always prevailing over **OCP**, **BRU** and/or **ACP**.[62] The observed post-precipitation of **HAP** takes place under alkaline conditions, after the quantitative precipitation of **BRU**. Then, the **OCP**/**HAP** formation onto the **BRU** surface process can be summarized as an alkali driven partial dissolution-reprecipitation reaction, in coincidence with the second base consumption event recorded at 450 min. FESEM images revealed at this early

10.1002/chem.202005483

stage of surface maturation, the occurrence of aligned arrays of spheroids. These surface events take place along lines that form an angle of 120º, fully coincident with the characteristic value formed between the crystallographic *a* and *c* directions of **BRU** lattice (see Figure S7). The preferential nucleation of **HAP** occurs at these inherently reactive terraces and borders, were dissolution is kinetically favoured due to the unsaturated coordination.[63] These observations confirm the recent claims regarding the intermediary role of **BRU** phase in biomineralization process.[64] In the case of **ACP**, the birth of randomly distributed flakes onto the surface was also noticed after the precipitation (see Figure S8), according to related systems.[65] However, in contrast with **BRU**, these nanoparticles are massively consumed to form **HAP**/**OCP** phases in an alkali driven dissolution-reprecipitation reaction. It must be highlighted from this initial screening the necessity to stabilize **ACP** from recrystallization aiming to preserve the amorphous nature of this desired phase.

**2. Stabilization and size control of ACP employing viscous cosolvents.**

Once established the conditions to avoid the formation of **BRU**, we decide to move forward in the search of alternative precipitation conditions to favour the obtainment of **ACP** and prevent its transformation into the more stable **HAP**. In general terms, the growth of **ACP** is favoured employing fast precipitations process and high oversaturation values.[53] However, the crystallization of **BRU** is markedly fast and prevails even under oversaturated systems.[39] As was mentioned before, many strategies were proposed in literature to stabilize **ACP** phases from recrystallization. However, herein we explored a novel alternative to stabilize **ACP**, keeping in mind to preserve the pristine surface and chemical properties of these particles. Theoretically, decreasing precipitation temperature and/or employing alternative cosolvents, could affect the inherent phase stability (solubility) of the solid products and their (re)crystallization kinetics as well, paving the way towards the obtaining of **ACP**. In the current context, both strategies can be easily implemented with the *Epoxide Route* since this method offers the possibility to drive the alkalinization process by employing a variety of nucleophiles,[33] epoxides[66] and/or solvents.[47] Hence, as a first step to obtain stable **ACP** the effect of temperature was evaluated under a markedly lower precipitation/(re)crystallization scenario (5 ºC). At these conditions the chloride driven alkalinization rate decreases to a tenth of the value recorded at 25 ºC.[47] therefore, the synthetic protocol must be adjusted to ensure quantitative precipitation within a few hours. This can be obtained either by increasing the chloride and/or glycidol concentration, or even by employing a more polarizable or stronger nucleophile. Since iodide has been proven to increase almost 25 times the ring-opening reaction in comparison with chloride,[33] the alkalinization rate can be easily increased, even under this low temperature scenario, with small amounts of iodide without increasing significantly ionic strength. Thereby, we decide to perform the precipitation of calcium phosphate phases by replacing chloride by iodide. Figure 4 depicts the FESEM images of the samples obtained from 24h aged solutions. For all the evaluated calcium concentration, the prevalence of spheroids larger than 500 nm in diameter is observable (Figure S9-S10 and Table S1); the lack of nanoflakes and the recorded PXRD patterns confirmed the effective prevention of recrystallization from **ACP** into **HAP** or **HAP** + **OCP** mixtures (see Figure S11). Thus, this low-temperature precipitation approach successfully allows the obtainment of **ACP** in the form of micrometric spheres. Nevertheless, these samples need to be dried or stored at low temperature in order to avoid subsequent recrystallization processes. Beyond this successful result, the *Epoxide Route* was conceived to be a simple and easy synthesis procedure, being the refrigerated handling of the obtained colloids a major operational drawback.

10.1002/chem.202005483

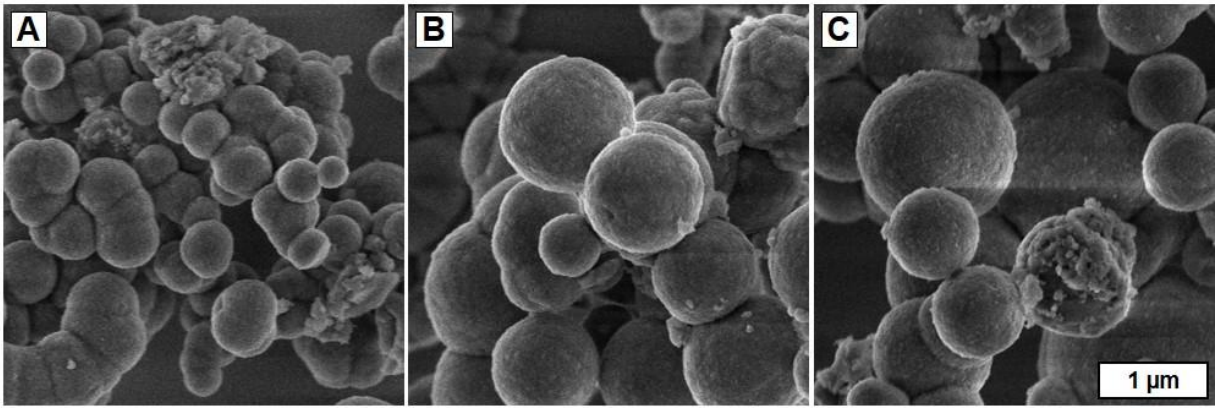


**Figure 4.** FESEM images for samples obtained by aging 24h at 5 °C aqueous solutions containing: [Ca] = 4 (A), 5 (B) and 6 mM (C), [$H_3PO_4$] = 2.4, 3.0 and 3.6 mM, [NaI] = 100 mM and and [Gly] = 138 mM. Scale bar represents 1 µm for all images.

Then, the use of other cosolvents was evaluated to preserve a key asset of the *Epoxide Route* which lies in the possibility of working at room temperature. As a first step, the effect of the solvent on the alkalinization rate was investigated. Figure S12 presents the pH profiles of solutions containing fixed concentrations of NaCl and Gly and increasing initial amounts of EtOH. The higher the ethanol amount the faster the alkalinization rate. This result can be understood considering that the reduction of percentage of water (by increasing the amount of other cosolvent) preferentially decreases the epoxide hydrolysis rate which always competes with the alkalinization (halohydrin formation). In addition, this effect does not depend on the nature of the cosolvent as it was proved by using glycerine instead of EtOH (see Figure S13).

In line with that, precipitation experiments were carried out by employing ethylene glycol (EG) or glycerine (GL) as cosolvents at $A_W(\%) = 25\%$, under two alkalinization rates. Figure 5 depicts the FESEM images of the obtained samples. For all samples obtained at $A_W(\%) = 25\%$, the occurrence of spheroidal nano-microparticles with no nanoflakes prevails, irrespective of the chosen cosolvents and/or alkalinization rate. PXRD confirms their amorphous nature (Figure S14). Hence, these results indicate that under these synthetic conditions **ACP** can be easily obtained at room temperature. Interestingly, at this condition – $A_W(\%) = 25\%$ – the employed cosolvent seems to be an effective tool to tune the size of the **ACP** nanoparticles. As pointed out, the alkalinization rate does not depend on the nature of the cosolvent, thus this effect must be related with the physicochemical properties of the cosolvent itself, exclusively.

10.1002/chem.202005483

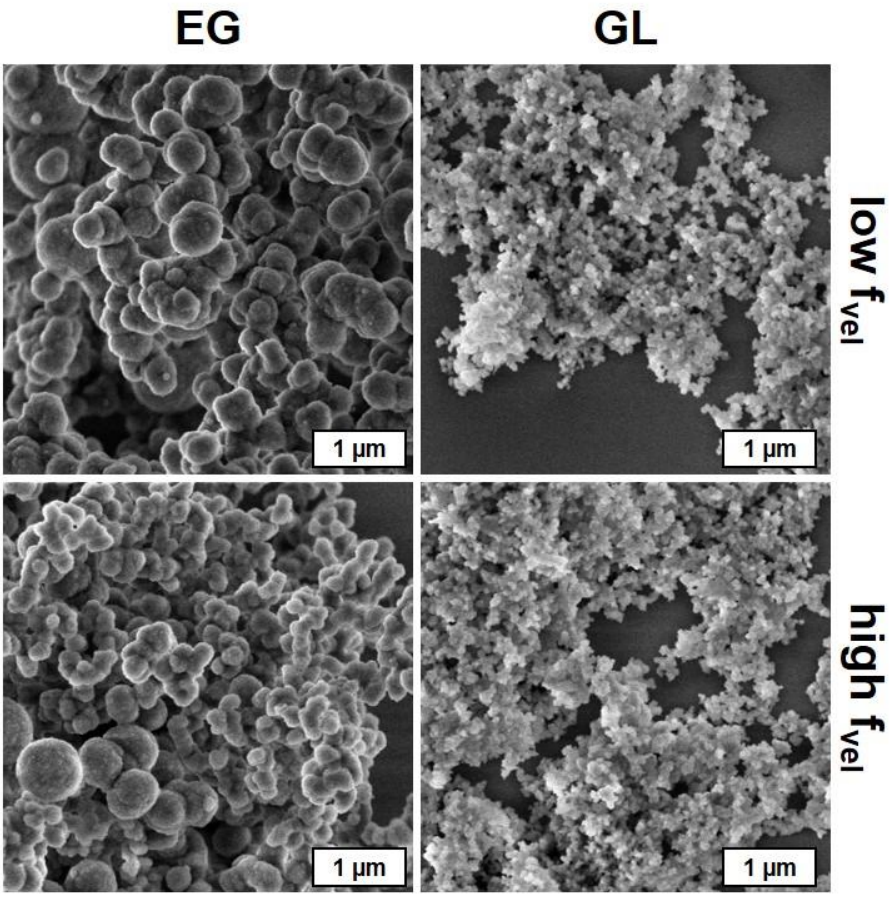


**Figure 5.** FESEM images for samples obtained by aging 24h at room temperature solutions containing: [Ca] = 5 mM, [$H_3PO_4$] = 3 mM, [$Cl^-$] = 100 mM and, [Gly] = 516 (low $f_{vel}$) and 2580 mM (high $f_{vel}$) and ethylene glycol (EG – left panel) or glycerine (GL – right panel) as cosolvent at $A_W(\%) = 25\%$.

In order to unveil the role of the cosolvent regarding the size of the **ACP** nanoparticles, a set of samples was prepared with ternary water–EG–GL solutions, keeping a constant value $A_W(\%) = 25\%$ and varying the EG to GL ratio. Figure 6 depicts the FESEM images of the obtained samples being possible to observe that while spheroidal NP of *ca.* 530 ± 190 nm are obtained for pure EG (Figure 6A), significantly smaller NP of around 60 ± 11 nm prevail for pure GL (Figure 6F). Indeed, the size can be tuned on demand by varying EG:GL ratio (see Figure S15-S17 and Table S4), ensuring the expected amorphous nature (see Figure S18).

10.1002/chem.202005483

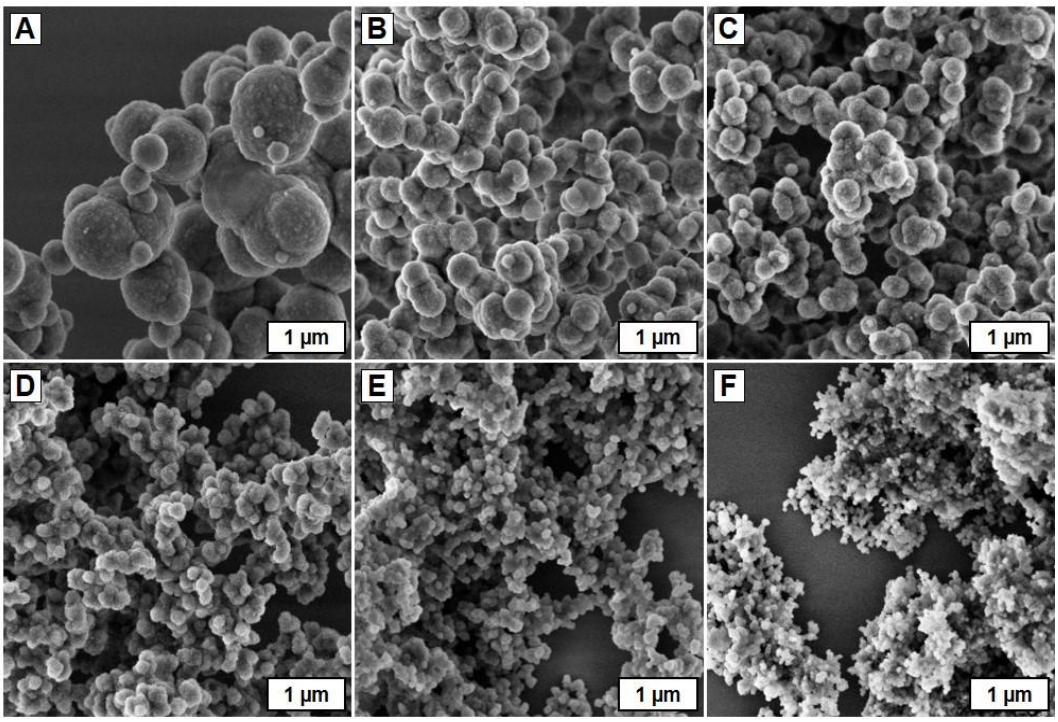


**Figure 6.** FESEM images of samples obtained after aging 24h at room temperature solutions containing: [Ca] = 5 mM, [$H_3PO_4$] = 3 mM, [$Cl^-$] = 100 mM and, [Gly] = 516 mM at $A_W(\%) = 25\%$. The amount of cosolvent was tuned from pure EG (0%) to pure GL (100%). $GL(\%)$ calculated as: $GL(\%) = \frac{V_{GL}}{V_{GL}+V_{EG}} \cdot 100$, are 0% (A), 20% (B), 40% (C), 60% (D), 80% (E) and 100% (F).

It should be noted that at this point we are able to obtain **ACP** nanoparticles controlling the size and preventing the occurrence of **HAP** or **HAP** + **OCP** transformation. As a complementary characterization, attenuated total reflectance Fourier-transform infrared spectroscopy (ATR-FTIR) was performed on the solid samples to evaluate the eventual presence of the employed cosolvents. Figure S19 depicts almost indistinguishable spectra between the samples obtained in pure water with those obtained with either EG or GL, confirming the absence of cosolvent molecules on the surface of the **ACP** nanoparticles. The weak signals registered between 1300 and 1600 $cm^{-1}$ indicate an incipient incorporation of carbonate that stands below 10% of the saturation values reported for related phases aged in carbonate rich solutions.[67] [68] Thermal decomposition of water and EG-based **ACP** samples follow an identical trace, irrespective of the employed cosolvent (see Figure S20). Assuming that the weakly occluded water is mostly removed below 100 ºC and the strongly bound water is lost between 200 and 400 ºC,[69] the hydrated **ACP** phase can be properly depicted according to the $Ca_3(PO_4)_2 \bullet 1.3H_2O$ formula.

Once prepared, the **ACP** colloidal suspensions can be stored at room temperature for months in this green and biocompatible solvent mixture guaranteeing the lack of phase transformation.

Additionally, a simple washing process ensures cosolvent removal returning the expected high reactivity of "naked surface" of **ACP** nanoparticles, when necessary.

Being established the ability of this method to obtain **ACP** with a precise control over the particle size, a complementary exploration based on Small/Wide Angle X-ray Scattering (SAXS/WAXS) was performed to shed light on the role of the solvent on the internal structure (further information can be found in 'SAXS section' in Supporting Information). Since particle size distribution for most of the samples were above the maximum range achievable by SAXS (>100-150 nm), the geometry was optimized to analyse its internal structure, meaning the microstructure. Figure 7A depicts the SAXS patterns registered for samples obtained for increasing $GL(\%)$ values. Nanometric electron density inhomogeneities are observed as a clear feature at large angle's value. These inhomogeneities are compatible with (nano)particles composed by small primary units. In terms of Guiner-Porod analysis the equivalent diameters of these units can be estimated as a weighted average, where large entities scatter more than small ones (further details in Section SAXS, Supporting Information). In concordance with the reduction on the (nano)particle size estimated by SEM (Figure 6), the primary unit size experiments a progressive reduction from 2.6 to 2.1 nm, for synthesis carried out by employing $GL(\%)$ values from 0 to 40%. In the case of $GL(\%) \geq 60\%$, these primary units were not observed, probably due to its small size (<1.5 nm). However, these samples present fractal like structures, where the increments in $GL(\%)$ values promote a reduction in the fractal correlation length, which is proportional to $d_{eq}$ (Figure 7B). Interestingly, for samples synthesized at $GL(\%) < 40\%$ the fractal nature is lost, although nanoparticles are still amorphous (PXRD and WAXS measurements. Figure S18). Thus, the growth and consolidation of primary units lead to a decrease in fractal dimension (f) with an increase in fractal correlation length ($\xi$) where $d_{eq} \propto [0.5 \cdot f(1+f)]^{1/2}\xi$ and average particle size observed by SEM (Figure 6).

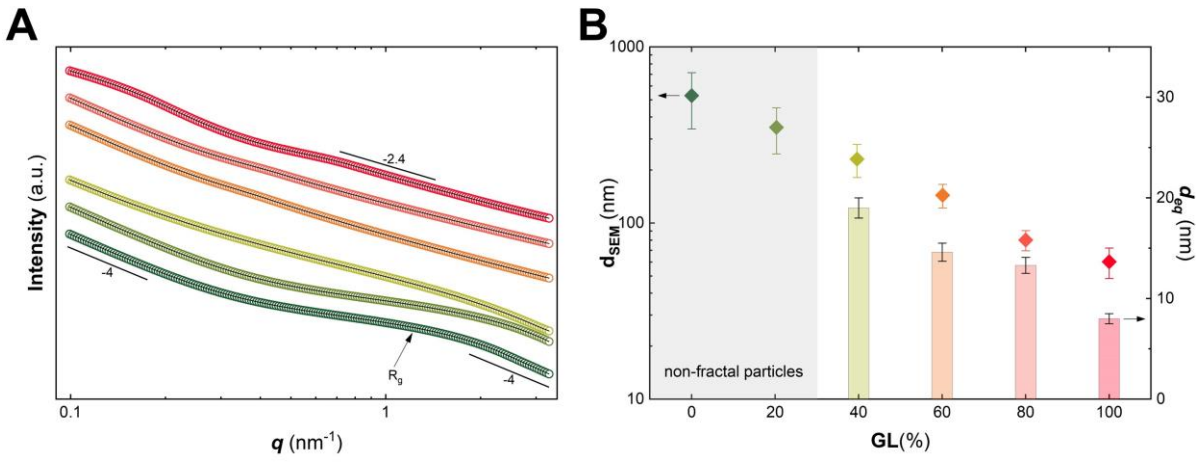

**Figure 7.** SAXS patterns expressed in *loglog* scale as a function of $GL(\%)$ with 0% at the bottom (in green) and 100% at the top (in red) (A). Dependence of average particle size obtained from SEM (diamonds) and equivalent diameter ($d_{eq}$) from the larger fractal aggregates obtained from Guiner-Porod fitting procedure (bars) as a function of $GL(\%)$. More details can be found in Section SAXS, in SI.

The particles obtained with the present method can be rationalized in terms of the growing mechanism of **ACP** in aqueous media.[70] [71] [72] According to recent studies,[73] well-defined spheroidal molecular precursors of 0.9 nm in diameter, known as *Posner* clusters, [10] obeying to the formula $Ca_9(PO_4)_6 \bullet nH_2O$ are the primary building units of **ACP**. These moieties have a minor abundance in solution, compared to the prevalent calcium and phosphate free ions, and neutral $CaHPO_4 \bullet nH_2O$ ion pairs. However, close to the pH values of precipitation these dense clusters, increase their concentration with pH while reach a neutral condition (total deprotonation) and subsequently aggregate in a non-ordered fashion, giving birth to **ACP** particles. Moreover, a detailed inspection of the SAXS patterns suggests that the set of **ACP** samples can be divided in two main groups, according to their fractal or non-fractal nanostructures.

The SAXS analysis of the particles obtained in the presence of EG and/or GL cosolvents suggests a partially hindered **ACP** precipitation process that operates at two levels, modifying (*i*) the structure and size of primary units and (*ii*) limiting the growth of the final particles as well. In the case of EG-rich based solutions, the dense primary particles of *ca.* 2.6 nm can be interpreted as a set of few *Posner* clusters that condensed in the form of these dense nano entities, that further agglomerate into large secondary **ACP** particles. In contrast, GL-rich based solutions primary units coalesce in the form of open fractals. Notwithstanding, these fractal arrays of primary units also agglomerate into larger final **ACP** particles with a markedly smaller (one order of magnitude) diameter.

Hence, the combination of EG and GL effectively modulates the **ACP** growth, tuning either size and/or microstructure in a broad range, starting from small highly fractalized nanoparticles, up to micrometric spheroids that are more than an order of magnitude larger. Interestingly, these cosolvents hinder the release of *Posner* clusters from **ACP** to liquid media, preventing their rearrangement and the heterogeneous nucleation of nano-crystalline **HAP**[1] or related phases as **OCP**, that governs the maturation process in pure aqueous media.[20] [74] Hence, these results introduce the use of viscous green and biocompatible cosolvents as a new tool to control **ACP** particle size and at the same time to inhibit massive recrystallization.

## Conclusions

Beyond the established versatility for the synthesis of nanomaterials, the *Epoxide Route* offers a straightforward screening tool to identify the sequence and length of the most significant precipitation steps of typical metastable calcium phosphates as **ACP** or **BRU**, including the occurrence of post precipitation events and related phase transitions. In addition, this method can be adapted to a wide range of alternative conditions such as low temperature precipitation, in order to drive quantitative formation of stable **ACP** after suitable time scales.

Despite the marked effect of cosolvent addition on the alkalinization rate, this variable could have a minor effect on the nucleation and growth mechanism, that is mainly governed by the composition of the solvent mixture. This uncommon preparative variable demonstrated to be a suitable alternative to tune **ACP** particle size (and microstructure) in a wide range of diameters, while ensuring the chemical purity and the surface reactivity of these key nanobuilding blocks.

**Acknowledgements**

This work was supported by the University of Buenos Aires (UBACyT 20020130100610BA for MJ), the Agencia Nacional de Promoción Científica y Tecnológica (ANPCyT PICT 2012-1167 for MJ and PICT 2017-3150 for CHI) and the National Research Council of Argentina (CONICET PIP 11220170100991CO for MJ). VO is a member of ALN. MJ and CHI are Research Scientists of CONICET (Argentina). This research team wants to highlight the dedicated effort of reviewers that enhanced the experimental approaches and the overall discussion as well.

**Keywords**

amorphous nanoparticles; calcium phosphates; epoxide route; microstructure; synthesis

## References

[1] A. Lotsari, A. K. Rajasekharan, M. Halvarsson and M. Andersson, *Nature Communications* **2018**, *9*, 4170.
[2] D. Xiao, J. Zhang, C. Zhang, D. Barbieri, H. Yuan, L. Moroni and G. Feng, *Acta Biomaterialia* **2020**, *106*, 22-33.
[3] S. V. Dorozhkin and M. Epple, *Angewandte Chemie International Edition* **2002**, *41*, 3130-3146.
[4] D. Huang, B. He and P. Mi, *Biomaterials Science* **2019**, *7*, 3942-3960.
[5] D. J. Perez Enriquez, M. L. Dell' Arciprete, M. L. Dittler, A. Miñan, E. Prieto and M. C. Gonzalez, *New Journal of Chemistry* **2020**, *44*, 7541-7551.
[6] S. V. Dorozhkin, *Acta Biomaterialia* **2010**, *6*, 4457-4475.
[7] V. Uskoković and D. P. Uskoković, *Journal of Biomedical Materials Research Part B: Applied Biomaterials* **2011**, *96B*, 152-191.
[8] *BCC Publishing* **2008**, *143*.
[9] H. P. Rim, K. H. Min, H. J. Lee, S. Y. Jeong and S. C. Lee, *Angewandte Chemie International Edition* **2011**, *50*, 8853-8857.
[10] A. S. Posner and F. Betts, *Accounts of Chemical Research* **1975**, *8*, 273-281.
[11] R. Gelli, F. Ridi and P. Baglioni, *Advances in Colloid and Interface Science* **2019**, *269*, 219-235.
[12] V. M. Wu, S. Tang and V. Uskoković, *ACS Applied Materials & Interfaces* **2018**, *10*, 34013-34028.
[13] W.-X. He, A. K. Rajasekharan, A. R. Tehrani-Bagha and M. Andersson, *Advanced Materials* **2015**, *27*, 2260-2264.
[14] W. He, Y. Fu and M. Andersson, *Journal of Materials Chemistry B* **2014**, *2*, 3214-3220.
[15] M. Schweikle, S. H. Bjørnøy, A. T. J. van Helvoort, H. J. Haugen, P. Sikorski and H. Tiainen, *Acta Biomaterialia* **2019**, *90*, 132-145.
[16] E. Boanini, M. Gazzano and A. Bigi, *Acta Biomaterialia* **2010**, *6*, 1882-1894.
[17] I. Buljan Meić, J. Kontrec, D. Domazet Jurašin, A. Selmani, B. Njegić Džakula, N. Maltar-Strmečki, D. M. Lyons, M. Plodinec, M. Čeh, A. Gajović, M. D. Sikirić and D. Kralj, *CrystEngComm* **2018**, *20*, 35-50.
[18] Y. Li and W. Weng, *Journal of Materials Science: Materials in Medicine* **2007**, *18*, 2303-2308.
[19] J.-H. Han and S. Chung, *Applied Chemistry for Engineering* **2018**, *29*.
[20] S. Jiang, W. Jin, Y.-N. Wang, H. Pan, Z. Sun and R. Tang, *RSC Advances* **2017**, *7*, 25497-25503.
[21] N. Nassif, F. Martineau, O. Syzgantseva, F. Gobeaux, M. Willinger, T. Coradin, S. Cassaignon, T. Azaïs and M. M. Giraud-Guille, *Chemistry of Materials* **2010**, *22*, 3653-3663.
[22] K. Kandori, A. Yasukawa and T. Ishikawa, *Chemistry of Materials* **1995**, *7*, 26-32.
[23] J. Tao, W. Jiang, H. Pan, X. Xu and R. Tang, *Journal of Crystal Growth* **2007**, *308*, 151-158.
[24] M. Jobbágy, M. A. Blesa and A. E. Regazzoni, *Journal of Colloid and Interface Science* **2007**, *309*, 72-77.
[25] M. J. Hortigüela, M. C. Gutiérrez, I. Aranaz, M. Jobbágy, A. Abarrategi, C. Moreno-Vicente, A. Civantos, V. Ramos, J. L. López-Lacomba, M. L. Ferrer and F. Del Monte, *Journal of Materials Chemistry* **2008**, *18*, 5933-5940.
[26] M. Michel, M. Winterhalter, L. Darbois, J. Hemmerle, J. C. Voegel, P. Schaaf and V. Ball, *Langmuir* **2004**, *20*, 6127-6133.
[27] E. Colaço, D. Brouri, C. Méthivier, L. Valentin, F. Oudet, K. El Kirat, C. Guibert and J. Landoulsi, *Journal of Colloid and Interface Science* **2020**, *565*, 43-54.
[28] I. Sondi and E. Matijevic, *Journal of Colloid and Interface Science* **2001**, *238*, 208-214.
[29] I. Ortega, M. Jobbágy, M. L. Ferrer and F. Del Monte, *Chemistry of Materials* **2008**, *20*, 7368-7370.

[30] M. C. Gutierrez, M. Jobbagy, M. L. Ferrer and F. del Monte, *Chemistry of Materials* **2008**, *20*, 11-13.
[31] V. Oestreicher and M. Jobbágy, *Langmuir* **2013**, *29*, 12104-12109.
[32] V. Oestreicher, I. Fábregas and M. Jobbágy, *Journal of Physical Chemistry C* **2014**, *118*, 30274-30281.
[33] V. Oestreicher, D. Hunt, R. Torres-Cavanillas, G. Abellán, D. A. Scherlis and M. Jobbágy, *Inorganic Chemistry* **2019**, *58*, 9414-9424.
[34] N. Arencibia, V. Oestreicher, F. A. Viva and M. Jobbágy, *RSC Advances* **2017**, *7*, 5595-5600.
[35] A. E. Gash, T. M. Tillotson, J. H. Satcher Jr, J. F. Poco, L. W. Hrubesh and R. L. Simpson, *Chemistry of Materials* **2001**, *13*, 999-1007.
[36] V. Oestreicher, M. Perullini and M. Jobbágy, *Dalton Transactions* **2016**, *45*, 9920-9924.
[37] V. Oestreicher, C. Huck-Iriart, G. Soler-Illia, P. C. Angelomé and M. Jobbágy, *Chemistry – A European Journal* **2020**, *26*, 3157-3165.
[38] N. Tarutani, Y. Tokudome, M. Jobbágy, G. J. A. A. Soler-Illia and M. Takahashi, *Journal of Materials Chemistry A* **2019**, *7*, 25290-25296.
[39] Y. Tokudome, A. Miyasaka, K. Nakanishi and T. Hanada, *Journal of Sol-Gel Science and Technology* **2011**, *57*, 269-278.
[40] N. Tarutani, Y. Tokudome, M. Fukui, K. Nakanishi and M. Takahashi, *RSC Advances* **2015**, *5*, 57187-57192.
[41] Y. Tokudome, M. Fukui, N. Tarutani, S. Nishimura, V. Prevot, C. Forano, G. Poologasundarampillai, P. D. Lee and M. Takahashi, *Langmuir* **2016**, *32*, 8826-8833.
[42] N. Tarutani, Y. Tokudome, M. Jobbágy, F. A. Viva, G. J. A. A. Soler-Illia and M. Takahashi, *Chemistry of Materials* **2016**, *28*, 5606-5610.
[43] N. Tarutani, Y. Tokudome, M. Jobbágy, G. J. A. A. Soler-Illia, Q. Tang, M. Müller and M. Takahashi, *Chemistry of Materials* **2019**, *31*, 322-330.
[44] V. Oestreicher and M. Jobbágy, *Chemistry – A European Journal* **2019**, *25*, 12611-12619.
[45] V. Oestreicher, D. Hunt, C. Dolle, P. Borovik, M. Jobbágy, G. Abellán and E. Coronado, *Chemistry – A European Journal* **2020**, *27*, 921-927.
[46] V. Oestreicher, D. Hunt, M. Mizrahi, F. G. Requejo and M. Jobbágy, *Chemistry – A European Journal* **2020**, *26*, 17081-17090.
[47] V. Oestreicher and M. Jobbágy, *Chemical Communications* **2017**, *53*, 3466-3468.
[48] E. M. Flaten, M. Seiersten and J.-P. Andreassen, *Journal of Crystal Growth* **2009**, *311*, 3533-3538.
[49] D. Konopacka-Łyskawa, B. Kościelska and J. Karczewski, *Journal of Crystal Growth* **2015**, *418*, 25-31.
[50] D. Konopacka-Łyskawa, B. Kościelska and J. Karczewski, *Journal of Crystal Growth* **2017**, *478*, 102-110.
[51] D. B. Trushina, T. V. Bukreeva and M. N. Antipina, *Crystal Growth & Design* **2016**, *16*, 1311-1319.
[52] V. Oestreicher, C. Dolle, D. Hunt, M. Fickert and G. Abellán, *Nano Materials Science* **2020**, https://doi.org/10.1016/j.nanoms.2020.1012.1004.
[53] V. Uskoković, *Crystal Growth & Design* **2019**, *19*, 4340-4357.
[54] P. F. Schofield, K. S. Knight, J. A. M. v. d. Houwen and E. Valsami-Jones, *Physics and Chemistry of Minerals* **2004**, *31*, 606-624.
[55] S. Ucar, S. H. Bjørnøy, D. C. Bassett, B. L. Strand, P. Sikorski and J.-P. Andreassen, *Crystal Growth & Design* **2019**, *19*, 7077-7087.
[56] M. R. Christoffersen, J. Christoffersen and W. Kibalczyc, *Journal of Crystal Growth* **1990**, *106*, 349-354.
[57] A. L. Boskey and A. S. Posner, *The Journal of Physical Chemistry* **1973**, *77*, 2313-2317.
[58] Q. J. He and Z. L. Huang, *Journal of Crystal Growth* **2007**, *300*, 460-466.
[59] S. Jiang, H. Pan, Y. Chen, X. Xu and R. Tang, *Faraday Discussions* **2015**, *179*, 451-461.

[60] S. Jiang, Y. Chen, H. Pan, Y.-J. Zhang and R. Tang, *Physical Chemistry Chemical Physics* **2013**, *15*, 12530-12533.
[61] E. Fernández, F. J. Gil, M. P. Ginebra, F. C. M. Driessens, J. A. Planell and S. M. Best, *Journal of Materials Science: Materials in Medicine* **1999**, *10*, 169-176.
[62] M. Iijima, H. Kamemizu, N. Wakamatsu, T. Goto, Y. Doi and Y. Moriwaki, *Journal of Crystal Growth* **1998**, *193*, 182-188.
[63] M. Jobbágy and A. E. Regazzoni, *Applied Clay Science* **2011**, *51*, 366-369.
[64] J. Zhang, L. Wang and C. V. Putnis, *The Journal of Physical Chemistry B* **2019**, *123*, 2874-2881.
[65] P. G. Vekilov, *Nanoscale* **2010**, *2*, 2346-2357.
[66] Y. Tokudome, *Journal of the Ceramic Society of Japan* **2017**, *125*, 597-602.
[67] C. J. S. Ibsen, D. Chernyshov and H. Birkedal, *Chemistry – A European Journal* **2016**, *22*, 12347-12357.
[68] C. J. S. Ibsen, H. Leemreize, B. F. Mikladal, J. Skovgaard, M. Bremholm, J. R. Eltzholtz, B. B. Iversen and H. Birkedal, *Crystal Growth & Design* **2018**, *18*, 6723-6728.
[69] J. Vecstaudza, M. Gasik and J. Locs, *Journal of the European Ceramic Society* **2019**, *39*, 1642-1649.
[70] W. J. E. M. Habraken, J. Tao, L. J. Brylka, H. Friedrich, L. Bertinetti, A. S. Schenk, A. Verch, V. Dmitrovic, P. H. H. Bomans, P. M. Frederik, J. Laven, P. van der Schoot, B. Aichmayer, G. de With, J. J. DeYoreo and N. A. J. M. Sommerdijk, *Nature Communications* **2013**, *4*, 1507.
[71] D. Gebauer, M. Kellermeier, J. D. Gale, L. Bergström and H. Cölfen, *Chemical Society Reviews* **2014**, *43*, 2348-2371.
[72] A. Dey, P. H. Bomans, F. A. Muller, J. Will, P. M. Frederik, G. de With and N. A. Sommerdijk, *Nature Materials* **2010**, *9*, 1010-1014.
[73] A. Carino, C. Ludwig, A. Cervellino, E. Müller and A. Testino, *Acta Biomaterialia* **2018**, *74*, 478-488.
[74] L. Wang and G. H. Nancollas, *Chemical Reviews* **2008**, *108*, 4628-4669.